MULTI-MACHINE DETERMINATION OF SOL-TO-CORE MULTI-Z IMPURITY TRANSPORT IN ADVANCED CONFINEMENT REGIMES

N.T. HOWARD*, F. SCIORTINO
MIT Plasma Science and Fusion Center
Cambridge, MA, USA
Email: nthoward@psfc.mit.edu

T. ABRAMS, T. ODSTRCIL
General Atomics
San Diego, CA USA

F. SCOTTI, B. VICTOR
Lawrence Livermore National Lab
Livermore, CA, USA

B. GRIERSON, W. GUTTENFELDER, S. HASKEY, A. BORTOLON, F. EFFENBERG
Princeton Plasma Physics Lab
Princeton, NJ, USA

J. NICHOLS, S. ZAMPERINI
University of Tennessee – Knoxville
Knoxville, TN, USA

Abstract
Low to high-Z impurity transport spanning from the scrape-off-layer (SOL) to the plasma core has been studied on multiple US fusion devices in a wide range of confinement regimes. As part of the 2020 US Joint Research Target (JRT), 8 datasets obtained from Alcator C-Mod, DIII-D, and NSTX/NSTX-U were used to perform coordinated research to understand generation of impurities from material surfaces and their transport to the plasma core. In the SOL and divertor region, state-of-the-art SOL modelling of tungsten was validated against collector probe measurements, providing evidence for strong convective transport and for near-SOL impurity accumulation. Analytic modelling and spectroscopic measurements of tungsten erosion and re-deposition in the SOL indicated the importance of electric-field effects and gyro-motion in regulating prompt re-deposition. The first 3D modelling of boron SOL transport in DIII-D linked changes in parallel friction forces in the SOL to spatial boron distributions and qualitatively reproduced boron density asymmetries measured in the DIII-D divertor. Novel main ion charge exchange measurements combined with modelling displayed the role of impurity ionization and inward neoclassical convection of impurities in the recovery of the pedestal following ELMs. In the plasma core, cross-machine datasets were used to validate leading neoclassical and turbulent transport models and establish actuators for the regulation of core impurity transport in a wide range of plasma conditions. Flexible beam configurations on DIII-D were leveraged to definitively demonstrate the negligible role of roto-diffusion in impurity peaking in H-mode conditions. Comparison of cross-machine databases confirmed the robust correlation of impurity and electron density peaking and were used to validate both turbulent and neoclassical models, revealing areas of parameter space demonstrating strong agreement and disagreement with modelling. In a wide range of advanced operating regimes, neoclassical peaking of low & high-Z impurities was observed, and could be eliminated via modest central electron-heating, independent of regime and impurity studied. This paper presents a description of the experiments and analysis performed that help shed light on impurity dynamics in high confinement regimes.

1. INTRODUCTION

With the worldwide fusion program on the brink of transitioning to a new generation of fusion devices capable of generating burning plasma conditions and even producing electricity, the need for developing a comprehensive understanding of impurity generation and transport has shifted to the forefront of plasma physics research. In present day devices, impurities contribute to power balance but are often introduced only for targeted transport and seeding experiments. However, operation of burning plasma conditions will require impurities to take a more central role in device operation. Burning plasmas, by definition, contain a core source of impurities taking the form of helium ash from D-T fusion reactions. The harsh plasma environment created by burning plasma conditions will inevitably interact with the first wall, introducing metallic impurities into the plasma edge that may be transported to the hot fusion core; diluting the fuel, radiating energy, and reducing the reactor's performance. Furthermore, all of the energy generated by this system must be exhausted in a manner that does not destroy the divertor, requiring impurity seeding to manage heat and particle loads that will significantly exceed those in current devices. As a result, there is strong motivation to develop validated impurity transport models

that are capable of predicting impurity generation and transport from the reactor wall to the axis to inform operation of burning plasmas. The 2020 US Joint Research Target (JRT) was focused on the core to edge validation of impurity transport models across multiple US fusion devices. In this paper we present the analysis of 8 datasets obtained from 4 US fusion facilities (Alcator C-Mod, DIII-D, and NSTX/NSTX-U) that compare new measurements of impurity transport with cutting-edge models across the plasma minor radius.

2. SCRAPE-OFF-LAYER (SOL) IMPURITY TRANSPORT

To date, most analysis of impurity transport in the SOL has focused on the so-called near-SOL characterized by the region 1-2 characteristic density lengths from the separatrix. However, recent experiments and analysis on DIII-D utilized an outboard midplane, graphite rod collector probe (CP) to measure radial profiles of tungsten (W) deposition in the far-SOL during recent tungsten tracer experiments [1]. Measured deposition profiles of W demonstrate evidence of peaking along the edges of the collector probe, indicating the 3D nature of impurity transport in the far SOL. To facilitate analysis, a new 3D Monte Carlo code, 3DLIM [2] was developed and employed to model the W measurements in the far-SOL. T_e and n_e, obtained via plunging Langmuir probes during the experiments are inputs to 3DLIM. An impurity source is specified by the user and the impurity ions are launched from this region to simulate impurity transport from the near-SOL into the simulated far-SOL. The code then simulates a host of physical effects such as radial, parallel, and poloidal diffusion, convective transport, and parallel transport due to friction forces and follows the impurities until their deposition the CP probe surfaces. Measured W deposition and its comparison with 3DLIM are shown in Fig 1.

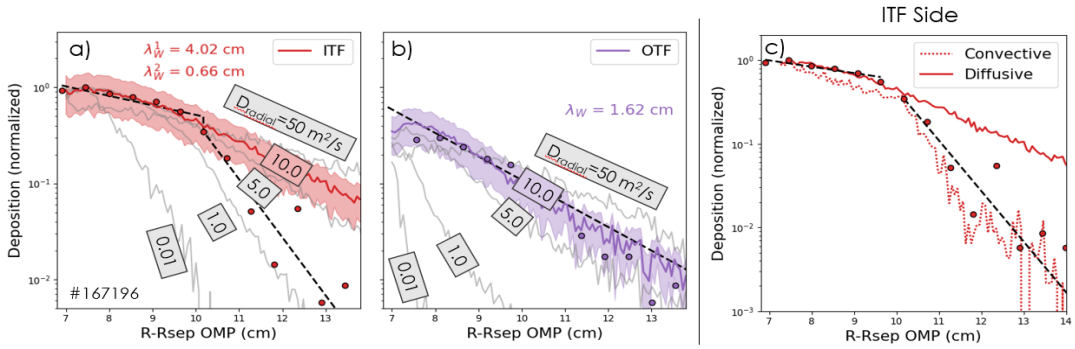

FIG 1. Reproduction of measured radial deposition profiles by 3DLIM (note log y-scale). Dots are RBS measurements, and lines with uncertainty bands are from 3DLIM simulation. a)-b): Effect of varying D_{radial} from 0.01 to 50 m^2/s is shown in grey, with the optimal value of 10 m^2/s in color. c): Diffusive versus convective radial transport is compared for ITF data.

Experimentally, W deposition on the outer target facing (OTF) side of the collector probe was found to decrease exponentially as one moves away from the separatrix. However, the inner target facing (ITF) side of the probe found an increase in the exponential decay of the data beyond R-R_{sep} = 10cm, which is where the connection length decreased by about a factor of 10. Initial analysis of this data tried to reproduce experimental measurements with the assumption of purely diffusive transport, scanning the value of assumed diffusion from 0.01 to 50 m^2/s. This analysis suggest that a diffusion coefficient of 10 m^2/s is best able to accurately reproduce the OTF collector probe data, while failing to capture the decreased decay length observed in data from the ITF side. However, purely convective radial transport (125 m/s) in 3DLIM produces simulation results that are in good quantitative agreement with the collector probe measurements on both the ITF and OTF side and predicts W deposition profiles along the length of the probe that are consistent with measurements. The origin for this behaviour is attributed to the fact that convective transport moves W ions through the far SOL at nearly constant speed, allowing the (connection length dependent) parallel flow to dominate the deposition on the CP [2]. In contrast, the random nature of the diffusive transport tends to flatten out the deposition profiles in the far-SOL. It is notable that the convective velocities inferred from 3DLIM are in rough quantitative agreement with the radial blob velocities measured in other experiments [3] [4]. In a separate set of experiments, the collector probe was inserted into nearly identical shots differing primarily in B_T direction. For conditions operating in the unfavourable B_T direction, the ratio of W deposition between the two sides was such that the ratio ITF/OTF > 1, with the opposite ratio observed in the favorable B_T direction. Coupled DIVIMP/3DLIM simulations indicate that reproduction of W deposition with ITF/OTF > 1 requires a long-hypothesized near-SOL impurity accumulation to form. Modeling also suggests that near-SOL impurity accumulation may not form in the favorable B_T direction due to fast inner target directed parallel plasma flows. Taken together, this analysis suggests that far-SOL impurity measurements can provide insight into near-SOL impurity dynamics, and that impurity transport in the far-SOL may best be modelled using radial convective transport. While not incorporated in the modelling of this section, convective ExB transport may help explain the requirement of radial convective transport, similar to that in [5].

In the absence of burning plasma conditions, the control of all impurities in fusion plasmas begins at the wall, where impurities are generated from the reactor first wall via processes such as chemical and physical sputtering. In present day fusion devices, it is well documented that the application of a thin coating of low-Z impurity to the first wall can significantly reduce impurity concentrations in the plasma core [6]. To achieve first wall conditioning, an impurity powder dropper was recently installed on the DIII-D tokamak, which has the potential to allow for in-situ, real-time growth of low-Z wall coatings [7][8]. Two DIII-D experiments were performed with the goals of 1.) establishing the effectiveness of powder dropping techniques including quantification of the boron powder amount needed to obtain favourable wall conditioning effects and 2.) utilize the DiMES system on DIII-D to characterize boron coatings as a function of the distance from the outer strike point and thus enabling study of the physics of the boron-rich wall layer.

The improvement of wall conditions was studied in a DIII-D plasma scenario operated in lower single null to provide optimal diagnostic coverage of the outer divetor target. Boron powder injection was introduced with incrementally increased quantities (2 – 20mg per discharge) into a series of discharges. To quantify the effect of the boron introduction on wall conditions, the ratios of carbon wall recycling/fueling (C_{wall}) and wall impurity carbon concentration (f_z in %) were chosen as the figures of merit. The wall condition parameter, $C_{wall} = \Gamma_D / \langle n_e \rangle$ is the ratio of the gas fueling divided by the achieved plasma density for repeat plasma discharges performed with the same pre-fill and density target trajectory, with higher values indicative of an improvement of wall conditions. The parameter f_z (%) is the carbon concentration (n_c / n_e) as measured in the plasma pedestal. The results from this sequence of plasma discharges are shown in Fig 2. An increase in the value of C_{wall} is observed as a result of the boron powder injection. There is not a clear reduction in the measured carbon concentration. However, as the dominant source of carbon is not fully understood, and may arise from main chamber interactions, it is not clear if boron coating of strike point targets should be expected to dramatically reduce the overall carbon content.

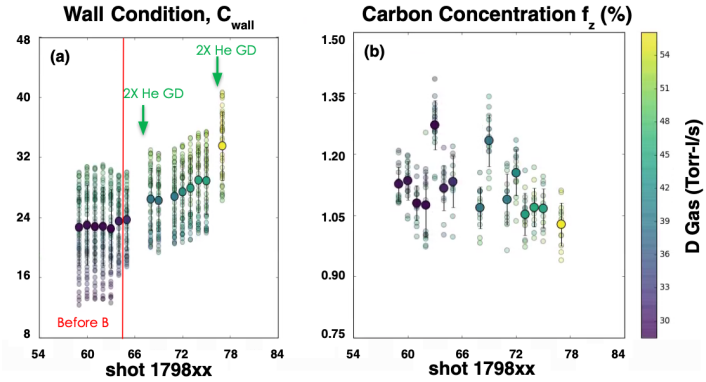

FIG 2.Wall conditioning parameter C_{wall} (a) and carbon concentration in the pedestal (b) for a sequence of DIII-D discharges with B powder injection.

Samples obtained from the DiMES probe were analysed to study the deposited boron layers. During these experiments the DiMES probe consisted of a W substrate located ~6cm from the OSP and oriented such the probe was flush with the divertor tiles. Upon removal of the exposed substrate, striations were clearly visible that were associated with the splitting of the strike point due to non-axisymmetric error fields. Laser Ablation Mass Spectroscopy was performed on the exposed substrate revealing that boron erosion and redeposition occur in 3D with a radial scale as small at 0.5 cm. EMC3-EIRENE [9] was employed to model the impurity transport and impurity fluxes to the divertor, enabling investigation into the role a toroidally localized boron source plays on the DiMES measured boron deposition patterns. These simulations indicate that a localized boron source can indeed lead to toroidally asymmetric boron flux at the divertor target. However, the spatial scales associated with these asymmetries are incompatible with the measured scales, suggesting the role of uncompensated error fields. Additional parameter scans were performed with EMC3-EIRENE that examined the dependence of results on plasma density. More uniform distributions of boron deposition are observed at low density with asymmetries arising at high density, resulting from an increased role of frictional flows at high density. These results suggest that low density scenarios represent more favorable targets for real-time boron power injection and point towards the need for 3D treatment to accurately model boron distribution in the SOL and divertor.

A recently developed UV spectroscopy system [10] was utilized to study *in-situ* re-deposition of tungsten (W) plasma facing components in DIII-D. Building off of previous work [11], and leveraging new rate coefficients, simultaneous evaluation of W gross erosion and local redeposition was achieved from the measurement of neutral and singly-ionized W lines obtained during the DIII-D metal rings campaign [12]. To analyze measurements obtained during this campaign, a simple picture of tungsten plasma material interactions was developed. In steady state this model can be summarized by equations for gross erosion and redeposition given by: $\Gamma_{gross} = (S_0/X_0B_0)\Phi_0$ and $\Gamma_{redep} = (S_1/X_1B_1)\Phi_1$. Here $\Phi_i = n_e n_i, X_i B_i$ where i = 0,1 represent the neutral and singly ionized charge states

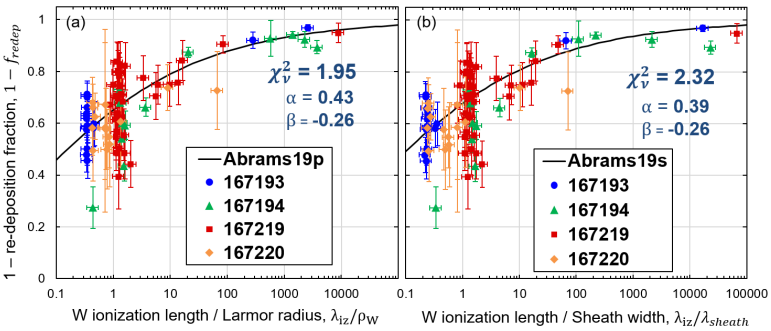

Fig 3. Calculated W prompt re-deposition fraction as a function of (a) iz/wand (b) iz/sh. The best-fit empirical scaling and the resulting parameters are overlaid in both cases.

and S_i, X_i, B_i are the ionization rate coefficient, excitation rate (for a given spectral line), and branching ratio respectively. 25 L-mode discharges were performed with the OSP placed on the W ring. These discharges span a large range of plasma conditions and therefore a wide range in W ionization lengths. Data from this discharge database was used to calculate the gross erosion and redeposition of W and the results were compared with calculations from other W redeposition models proposed by Guterl [13] and Naujoks [14] which predict that the W re-deposition scales with the width of the magnetic pre-sheath (λ_{iz}) and the W+ gyroradius (ρ_w) respectively. The data and the comparisons with these models are shown in Fig 3. From this data it is shown that the net erosion of tungsten near the outer strike point (OSP) is nearly equal to gross erosion rate when the neutral W ionization length is long (normalized to λ_{iz} and ρ_w). At these long neutral ionization lengths, both models appear to be in rough agreement with measurements. However, at lower relatively values of normalized ionization length, there is an inflection point observed in the data (around values of 2-3) that both models fail to capture. Since these measured values of erosion in this regime exceed that of the analytic models, this discrepancy could be ascribed to missing contributions to the W redeposition that occur due to more highly ionized charge states.

3. PEDESTAL IMPURITY TRANSPORT

Investigation of impurity dynamics was extended beyond the open field lines into the pedestal region to understand the transport of impurities from their source region into the plasma core. A series of low ELM frequency DIII-D discharges, operated in the absence of gas puffing, were used to study the processes by which impurities cross the pedestal and penetrate into the plasma core. Main-ion density measurements [15] were used in this work to enable a more straightforward interpretation of the dynamics, avoiding the complexities associated with the radial distribution of carbon charge states in the pedestal. Analysis of main ion and electron density measurements at different phases of the ELM cycle reveals that main ion densities do not track the time evolution of the electron density. The inter-ELM dynamics were found to occur in two phases i.) rapid initial recovery of main-ion and electron density followed by (ii) slower impurity and electron density build-up primarily attributed to impurity ionization and influx. This result is in contrast to the thermal and momentum transport channels, which display a prompt recovery and saturation following an ELM. ELM synchronized analysis performed on ELM-recovery data, with main ion densities computed using measured electron and carbon densities, and assuming a fully stripped carbon impurity, exhibit a peculiar a non-monotonic density feature occurring near the pedestal top as shown in Fig 4. Such a shape is inconsistent with purely diffusive particle transport as a locally positive main ion density gradient should drive transport into the core. However, such non-monotonic features may be possible [16] particularly where impurity transport was well-explained by neoclassical theory [17]

To better understand the role impurity dynamics during ELM recovery, the impurity transport code STRAHL [18] was used to calculate the self-consistent evolution of neoclassical transport coefficients and profiles. Inputs to the simulation were the experimental equilibrium, electron density, and ion and electron temperatures. The impurity source was adjusted to match the measured level of carbon and neoclassical transport coefficients were calculated using the NEOART [19] module within STRAHL. The dominant contribution to the neoclassical pinch is found to arise from Pfirsch-Schluter contributions. The inward pinch in the steep gradient region drives impurities into the plasma, reducing the main-ion density via quasineutrality in agreement with previous work [20]. A weaker screening of impurities is found inside the pedestal top, resulting in a buildup of carbon near the top of the pedestal. The magnitude of the inward pinch increases and the radial position of the pinch shifts inward as time evolves in the STRAHL simulation. The measured temporal dynamics in Fig 4. are consistent with the establishment of a neoclassical impurity pinch early in the ELM cycle, which preferentially favors inward impurity transport over main-ion fueling. Flattening the electron and main-ion density (by reduced recycling or increased opacity) reduces or even reverses the inward impurity pinch. The findings are largely consistent with results from both NSTX, NSTX-U and C-Mod, indicating the robust nature of the results

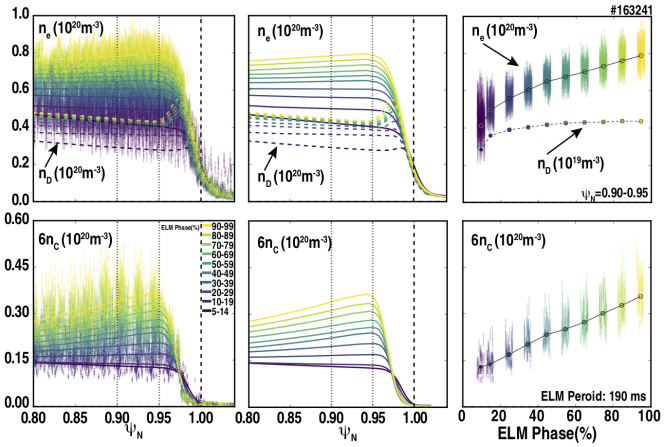

FIG. 4. ELM phase synchronized analysis of the pedestal recovery over 3.0 seconds of quasi-stationary conditions shown in space with (left) data and fits, (middle) fits only and (right) time evolution at top of pedestal. ELM phase has been divided into 10 segments and reveals dominance of carbon fueling beyond 20% into ELM cycle..

4. CORE IMPURITY TRANSPORT

The accumulation of impurities in the deep core has deleterious effects on plasma performance and must be avoided in fusion devices. Four cross machine datasets (Alcator C-Mod, DIII-D, NSTX/U) were used to validate leading transport models and establish actuators for the regulation of core impurity accumulation in a wide range of plasma conditions.

Mid-Z (Ca) impurity transport in the core of Alcator C-Mod was studied spanning the L, I, and H-mode confinement regimes. Trace calcium impurities were introduced via LBO in these confinement regimes and tracked using the spectrally resolved measurements of He-like Ca lines obtained using an X-ray Imaging Crystal Spectrometer (XICS) [21]. A new impurity transport code, Aurora, was developed from this work, building off of the successful STRAHL code with a new implementation that includes a Python interface, reduced file I/O, new algorithms, and coupling with Fortran and Julia to enable efficient parallel execution of impurity transport simulations. The MultiNest code [20] was used to perform Bayesian inference of impurity transport using ellipsoidal nested sampling algorithms on approximately 256 cores, performing on average more than 10M impurity transport model calls per inference. A new Bayesian Spectral Fitting Code (BSFC) was also applied to fit high-resolution spectral line features using truncated Hermite polynomial series, enabling higher-quality line brightness estimates from experimental data. The combination of these tools allowed for rigorous determination of impurity D and V profiles and their uncertainties as shown in Fig 5. for the I-mode discharge. Results were quantitatively compared with NEO, TGLF-SAT1 [22], and CGYRO [23] simulations. Impurity diffusion in the deep core was observed to be near the neoclassical level consistent with results from other worldwide fusion devices. Outside of the inversion radius, turbulence dominates. In this region reasonable agreement was found between inferred and simulated impurity diffusion (TGLF-SAT1 & CGYRO), under-predicting the magnitude of the inward pinch inferred from measurements. Sensitivity studies in relevant turbulent drive terms (a/L_{Ti}, ν_{ei}, a/L_n, T_i/T_e) displayed significant sensitivities within measurement uncertainties but did not appear to be able to resolve the discrepancy between modelling and experiment. Nonlinear CGYRO simulations were performed in the L, I and H-mode conditions at $\rho = 0.5$. These simulations demonstrated slight dependence of the impurity peaking on the effectively collisionality and were compared directly to an electron density peaking database spanning L, I, and H-mode. Although not yet conclusive, these results suggest a correlation between electron and impurity peaking, consistent with results found on other fusion devices.

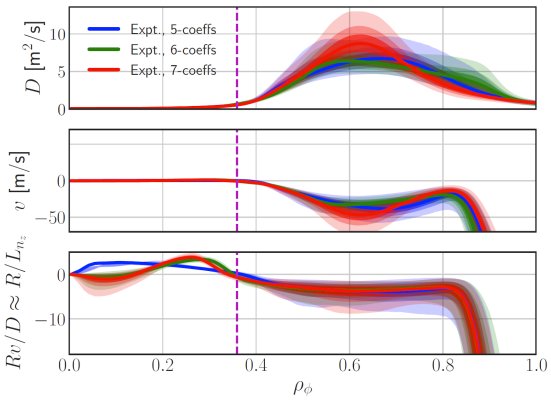

FIG 5. Ca (Z=20) transport coefficients inferred for a C-Mod I-mode discharge are shown for different numbers of radial spline coefficients

DIII-D's unique neutral beam configurations were leveraged to break typical correlations between rotation and other plasma parameters, enabling a novel investigation into the role of roto-diffusion in determining impurity peaking. This work created a database of 150+ ELM-y H-mode plasmas that were selected to best cover the parameter range accessible by the device. This database revealed strong correlations of a/L_{nc} with the local values of a/L_{Ti}, a/L_{ne} and weaker but non-negligible correlations with rotation gradient and T_e/T_i.

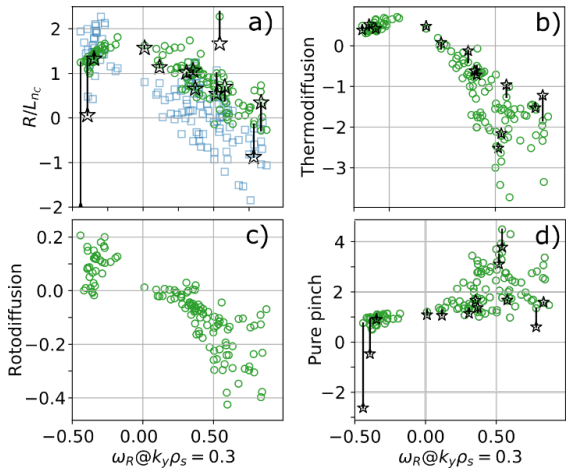

FIG 6. (a) Zero flux R/L_{n_C} from quasilinear (○) and nonlinear (★) gyrokinetics modeling, compared with experiment (□) (b) thermodiffusion $C_T R/L_{T_C}$, (c) rotodiffusion $C_u u'_C$ and (d) pure pinch C_p

A quasilinear estimate of the impurity peaking using the CGYRO code [24] was compared with measured a/L_{nc} values in Fig. 6a over the range of the database, revealing agreement between simulated and predicted scale lengths in TEM dominated conditions with a systematic underprediction found in ITG dominated conditions. The impurity flux Γ_C was decomposed in a diffusion flux, thermo-diffusion, roto-diffusion and pure pinch by following formula:

$$\frac{R\Gamma_C}{n_C} = D_C\left(\frac{R}{L_{n_C}} + C_T\frac{R}{L_{T_C}} + C_u u'_C + C_p\right)$$

Inward flux in ITG dominated regimes is driven by the pure pinch, and balanced by outward thermo-diffusion and roto-diffusion flux. Evaluation of impurity transport via nonlinear CGYRO simulation reached similar conclusions and was unable to explain discrepancies in the modelling.

The observed discrepancy motivated a detailed investigation of roto-diffusion, performed on DIII-D rotation scans. In contrast to previous work on JET and ASDEX, the DIII-D results indicate a negligible role of rotation on stationary carbon profiles and suggest that a balance of other pinch contributions likely explain DIII-D impurity peaking.

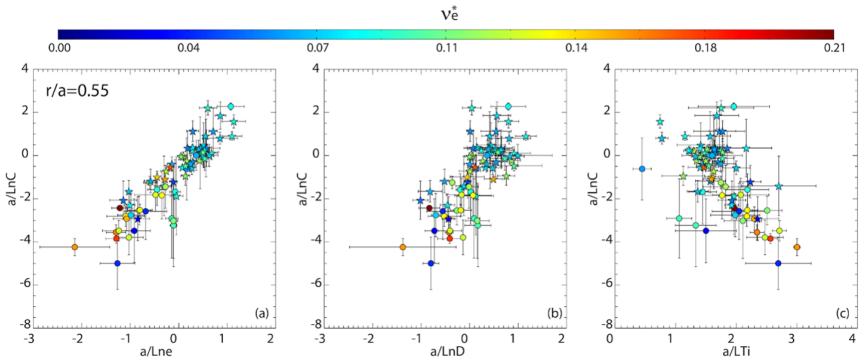

FIG. 7. a/L_{nC} as a function of a/L_{ne} (a), a/L_{nD} (b), a/L_{Ti} (c) evaluated at r/a=0.55 for the NSTX/NSTX-U database. Circles and stars represent discharges with boron and lithium conditioning, respectively

A similar carbon profile database was assembled on NSTX that was able to identify aspects of impurity transport that are common across both devices and operational regime. 66 H-mode discharges were identified that contained high quality profile data and measured intrinsic carbon profiles. Correlations between known turbulent and neoclassical drive terms and measured carbon scale lengths were investigated near mid radius, identifying positive correlation of a/L_{nc} with both a/L_{ne} and a/L_{nD} and a negative correlation with a/L_{Ti} (Fig. 7) The strong observed correlations with a/L_{ne} and a/L_{Ti} appear as a robust feature in both the DIII-D and NSTX/NSTX-U databases with the a/L_{ne} correlation also consistent with numerical modelling on Alcator C-Mod. However, measured carbon density gradients throughout the database are consistent with neoclassical transport as calculated by the NEO code [25]. This result is in contrast to DIII-D and Alcator C-mod where turbulence is believed to play a dominant role near mid radius. The effect of toroidal rotation on the impurity density was also evaluated with NEO. High levels of toroidal rotation (2 -3v_{th}) result in large poloidal asymmetries in the impurity density profile, which can lead to an enhancement of the neoclassical transport in the deep core. Poloidal asymmetries predicted by NEO were found to be in good agreement with measured asymmetry levels. Deviations from neoclassical transport are observed in the NSTX database for radial locations beyond mid radius (r/a = 0.65), with a clearly weaker than neoclassical peaking found in a set of discharges representing a collisionality scan and hollow impurity profiles measured for ELM-free lithium conditioned discharges, contrary to neoclassical modelling. In an attempt to resolve these discrepancies, linear CGYRO modelling was performed, revealing a mix of unstable modes ranging from microtearing at high collisionality to more prevalent ballooning type modes at lower collisionality. However, results from linear simulation appear unlikely to resolve discrepancies between measurement and modelling, indicating the need for a more comprehensive nonlinear analysis of the database.

A DIII-D database consisting of high-performance discharges was analysed to look for commonalities in impurity transport across confinement regimes and to probe the ability of ECH to regulate core impurity accumulation. This study examined a wide range of discharge conditions and impurity Z, including carbon, argon, and tungsten impurities. Neoclassical theory predicts that a change in direction of the impurity pinch will occur in the presence of a main ion density gradient exceeding half of the main-ion temperature gradient ($a/L_{nD} - 0.5\ a/L_{Ti}$) with positive values corresponding to an inward impurity pinch and negative values corresponding to screening. The analysis of experiments performed during the DIII-D W metal rings campaign showed an accumulation of W followed by a radiative collapse. NEO modelling of this discharge indicated that, inside of $\rho = 0.3$, ion thermal transport was at the neoclassical level and an inward directed impurity pinch was predicted. Subsequent discharges increased core deposited ECH at levels of 1.1, 2.0, and 3.2 MW. Analysis of these discharges is shown in Figure 8. These results suggest that both carbon and tungsten impurity peaking is reduced or eliminated when the neoclassical proxy is reduced to a value of 0.5 or below. Such conditions are found to occur with even a modest (~1MW) deposition of core ECH. The peaking/screening in the high q-min/steady state hybrid were both well-explained by the presence of a neoclassical impurity pinch in the plasma core. Taken together these results confirm previous work [26][27] demonstrating the role of neoclassical transport in the deep core and the ability of moderate ECH to reduce or eliminate impurity peaking, independent of the impurity Z.

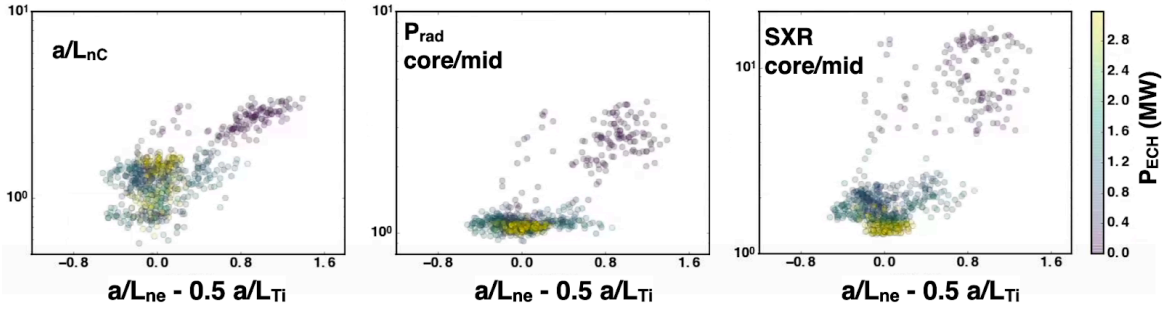

FIG. 8: (left) central carbon density inverse scale length a/L_{nC}. (middle) Ratio of central to outer bolometer channel. (right) Ratio of central to outer SXR channel. Data points are colored by ECH heating power.

5. CONCLUSIONS

This paper presented the analysis of multiple datasets that span confinement regime, plasma region, and device. The breadth of this work highlights the common features of impurity transport in tokamaks. The deep core of tokamaks is found to be dominated by neoclassical transport, with generally good agreement between modelling and inferred transport in this region. At larger major radii the transport of impurities appears to be dominated by turbulence, although it remains an open question as to whether reliable reproduction of impurity convection, and impurity peaking is possible with modern computational models. Large datasets of impurity peaking were created on multiple devices revealing a ubiquitous positive correlation of impurity peaking with a/L_{ne} and a negative correlation with a/L_{Ti} and the role of ECH in reducing on axis impurity accumulation was confirmed independent of Z and confinement regime. These studies indicate that neoclassical transport provides a good description of both dynamic and steady state impurity transport in the pedestal. This was confirmed on multiple devices and analysis revealed the role that impurity convection and ionization plays in pedestal recovery following an ELM crash. Modelling of impurities in the SOL and divertor demonstrated great progress with 3D models able to qualitatively and often quantitatively reproduce experimental measurements. Taken together, this work provides clear evidence of our progress in understanding core to edge impurity transport, reveals areas in need of additional research, and provides some confidence in our ability to predict impurities in future burning plasmas.

6. ACKNOWLEDGEMENTS:

This material is based upon work supported by the U.S. Department of Energy under Award(s) DE-FC02-04ER54698, DE-FC02-99ER54512, DE-AC02-09CH11466, DE-SC0014264, DE-AC05-00OR22725, DE-SC0019256, and DE-AC52-07NA27344

[1] DONOVAN, D., UNTERBERG, E., STANGEBY, P., ZAMPERINI, S., AUXIER, J., RUDAKOV, D., WAMPLER, W., ZACH, M., ABRAMS, T., DURAN, J., ELDER, J., NEFF, A., Utilization of outer-midplane collector probes with isotopically enriched tungsten tracer particles for impurity transport studies in the scrape-off layer of DIII-D, Rev. Sci. Instrum. vol. 89, pp. 10I115, (2018)

[2] ZAMPERINI, S., ELDER, J., STANGEBY, P., NICHOLS, J., DONOVAN, D., DURAN, J., UNTERBERG, E., RUDAKOV,D., Reproduction of collector probe deposition profiles using the far-SOL impurity transport code 3DLIM," Nucl. Mater. Energy, vol 25 100811, (2020)

[3] RUDAKOV, D., BOEDO, J., MOYER, R., STANGEBY, P., WATKINS, J., WHYTE, D., ZENG, L., BROOKS, N., DOERNER, R., EVANS, T., FENSTERMACHER, M., GROTH, M., HOLLMANN, E., KRASHENINNIKOV, S., LASNIER, C., LEONARD, A., MAHDAVI, M., MCKEE, G., MCLEAN, A., PIGAROV, A., WAMPLER, W., WANG, G., WEST, W., WONG, C., Far SOL transport and main wall plasma interaction in DIII-D, Nucl. Fusion vol. 45, pp. 1589–1599, (2005)
[4] LIPSCHULTZ, B., WHYTE, D., LABOMBARD, B., Comparison of particle transport in the scrape-off layer plasmas of Alcator C-Mod and DIII-D Plasma Phys. Control. Fusion. vol. 47, pp. 1559–1578, (2005)
[5] JAERVINEN, A., ALLEN, S., LEONARD, A., MCLEAN, A., MOSER, A., ROGNLIEN, T., SAMUELL, C., Role of poloidal E × B drift in divertor heat transport in DIII-D, Contrib. to Plasma Phys. 1–7. (2019) doi:10.1002/ctpp.201900111.
[6] BUZHINSKIJ, O.I., SEMENETS, Y.M., Review of in Situ Boronization in Contemporary Tokamaks, Fusion Technol, vol. 32, no. 1, pp. 1–13, (1997)
[7] BORTOLON, A., ROHDE, V., MAINGI, R., WOLFRUM, E., DUX, R., HERRMANN, A., LUNSFORD, R., MCDERMOTT, R.M., NAGY, A., KALLENBACH, A., MANSFIELD, D.K., NAZIKIAN, R., NEU, R., THE ASDEX UPGRADE TEAM, Real-time wall conditioning by controlled injection of boron and boron nitride powder in full tungsten wall ASDEX Upgrade, Nucl Mater Energy, vol. 19, pp.384–389, (2019)
[8] NAGY, A., BORTOLON, A., MAUZEY, D.M., WOLFE, E., GILSON, E.P., LUNSFORD, R., MAINGI, R., MANSFIELD, D.K., NAZIKIAN, R., ROQUEMOER, A.L. A multi-species powder dropper for magnetic fusion applications, Rev Sci Instrum, vol. 89, no. 10, p. 10K121, (2018)
[9] EFFENBERG, F., BORTOLON, A., FRERICHS, H., GRIERSON, B., LORE, J.D., ABRAMS, T., EVANS, T.E., FENG, Y., LUNSFORD, R., MAINGI, R., NAGY, A., NAZIKIAN, R., ORLOV, D., REN, J., RUDKOV, D.L., WAMPLER, W.R., WANG, H.Q., 3D modeling of boron transport in DIII-D L-mode wall conditioning experiments, Nucl. Mat. and Energy 26, 100900, (2021)
[10] JOHNSON, C.A., ENNIS, D.A, LOCH, S.D., HARTWELL, G.J., MAURER, D.A., ALLEN, S.L., VICTOR, B., SAMUELL, C., ABRAMS, T., UNTERBERG, E., Advances in neutral tungsten ultraviolet spectroscopy for the potential benefit to gross erosion diagnosis Plasma Phys. Control. Fusion vol. 61, pp. 095006, (2019)
[11] ABRAMS, T., Measurements of Tungsten Net Erosion in the DIII-D Divertor via WI and WII Spectroscopy and Comparison to Re-deposition Models, Nucl. Mater. Energy in preparation (2021)
[12] WAMPLER, W., RUDAKOV, D., WATKINS, J., MCLEAN, A., UNTERBERG, E., STANGEBY, P., Measurements of tungsten migration in the DIII-D divertor, Phys. Scr., vol. T170, pp. 014041, (2017)
[13] GUTERL, J., WAMPLER, W., RUDAKOV, D., ABRAMS, T., WANG, H., MCLEAN, A., SYNDER, P., Reduced model of high-Z impurity redeposition and erosion in tokamak divertor and its application to DIII-D experiments, Plas. Phys. Con. Fus., 61, 125015 (2019)
[14] NAUJOKS, D., ASMUSSEN, K., BESSENRODT,-WEBERPALS, M., DESCHKA, S., DUX, R., ENGLEHARDT, W., FIELD, A., FUSSMANN, G., FUCHS, J., GARCIA-ROSALES, C., Tungsten as target material in fusion devices, Nucl. Fus. Vol 36., 671 (1996)
[15] HASKEY, S., GRIERSON, B., STAGNER, L., CHRYSTAL, C., ASHOURVAN, A., BORTOLON, A., BOYER, M, BURRELL, K., COLLINS, C., GROEBNER, R., KAPLAN, D., PABLANT, N., Active spectroscopy measurements of the deuterium temperature, rotation, and density from the core to scrape off layer on the DIII-D tokamak, Rev. Sci. Instrum. 89 10D110, (2018)
[16] HASKEY, S., GRIERSON, BURRELL, K., CHRYSTAL, C., GROEBNER, R., KAPLAN, D., PABLANT, N., STAGNER, L., Measurement of deuterium density profiles in the H-mode steep gradient region using charge exchange recombination spectroscopy on DIII-D Rev. Sci. Instrum 87, 11E553, (2016)
[17] DELGADO-APARICIO, L., STUTMAN, D., TRITZ, K., FINKENTHAL, M., KAYE, S., BELL, R., KAITA, R., LEBLANC, B., LEVINTON, F., MENDARD, J, Impurity transport studies in NSTX neutral beam heated H-mode plasmas Nucl. Fusion 49 085028, (2009)
[18] DUX, R. "STRAHL User Manual" Max Planck Institut fur Plasmaphysik Report No. jpp 9/82, Garching, Germany, 2007
[19] PEETERS, A., Reduced charge state equations that describe Pfirsch Schlüter impurity transport in tokamak plasma, Phys. Plasmas 7, 268, (2000)
[20] CASALI, L., FABLE, E., DUX, R., RYTER, F., AND ASDEX UPGRADE TEAM, Modelling of nitrogen seeding experiments in the ASDEX Upgrade tokamak, Phy. Plasmas vol. 25,032506 (2018)
[21] REINKE, M., PODPALY, Y., BITTER, M., HUTCHINSON, I., RICE, J., DELGADO-APARICIO, L., GAO, C., GREENWALD, M., HILL, K., HOWARD, N., HUBBARD, A., HUGHES, J., PABLANT, N., WHITE, A., WOLFE, S. X-ray imaging crystal spectroscopy for use in plasma transport research, Rev of Sci Inst 83 , 113504 (2012)
[22] FEROZ, F., HOBSON, M., BRIDGES, M., MultiNest: an efficient and robust Bayesian inference tool for cosmology and particle physics, Monthly Notices of Royal Asto. Soc., Vol 398 (2009)
[23] STAEBLER, G., KINSEY, J., A theory-based transport model with comprehensive physics" Phys. Plasmas 14 (5), 055909 (2007)
[24] CANDY, J., BELLI, E., BRAVENEC, R., A high-accuracy Eulerian gyrokinetic solver for collisional plasmas, J. Comput. Phys. 324 , 73 (2016)
[25] BELLI, E., CANDY, J., Kinetic calculation of neoclassical transport including self-consistent electron and impurity dynamics, Plasma Phys. Control. Fusion 50 095010, (2008)
[26] DUX, R., NEU, R., PEETERS, A., PEREVERZEV, G., MUCK, A., RYTER, F., STOBER, J., ASDEX UPGRADE TEAM Influence of the heating profile on impurity transport in ASDEX Upgrade, Plas. Phys. Control. Fus., 45(9) 1815-1825 (2003)
[27] KALLENBACH, K., DUX, R., MAYER, M., NEU, R., PUTTERICH, T., BOBKOV, V., FUCHS, J., EICH, T., GIANNONE, L., GRUBER, O., Non-boronized compared with boronized operation of ASDEX Upgrade with full-tungsten plasma facing components, Nucl. Fus. 49(4) 045007 (2009)